The Astrophysical Journal, 1004:173 (16pp), 2026 June 20 https://doi.org/10.3847/1538-4357/ae69cc

TITAN DR1: An Improved, Validated, and Systematically Controlled Recalibration of ATLAS Photometry toward Type Ia Supernova Cosmology

Elijah G. Marlin[1], Yukei S. Murakami[2], Dillon Brout[1], Jack W. Tweddle[3], Brodie Popovic[4], Ken W. Smith[3,5], Stephen J. Smartt[3,5], Daniel M. Scolnic[6], David Jones[7], Erik R. Peterson[8,9], Adam G. Riess[2,10], Maria Vincenzi[3], Nora F. Sherman[11], Maria Acevedo[6], Jasper Milstein[1], Mitchell Dixon[7], and Armin Rest[2,10]
[1] Departments of Astronomy and Physics, Boston University, Boston, MA 02215, USA; emarlin@bu.edu
[2] Department of Physics and Astronomy, Johns Hopkins University, Baltimore, MD 21218, USA; ymuraka2@jhu.edu
[3] Astrophysics sub-Department, Department of Physics, University of Oxford, Keble Road, Oxford, OX1 3RH, UK
[4] School of Physics and Astronomy, University of Southampton, Southampton, SO17 1BJ, UK
[5] Astrophysics Research Centre, School of Mathematics and Physics, Queen's University Belfast, BT7 1NN, UK
[6] Department of Physics, Duke University, Durham, NC 27708, USA
[7] Institute for Astronomy, University of Hawai'i, 640 N. A'ohoku Pl., Hilo, HI 96720, USA
[8] Department of Physics, University of Michigan, Ann Arbor, MI 48109, USA
[9] Society of Fellows, University of Michigan, Ann Arbor, MI 48109, USA
[10] Space Telescope Science Institute, Baltimore, MD 21218, USA
[11] Institute for Astrophysical Research, Department of Astronomy, Boston University, 725 Commonwealth Avenue, Boston, MA 02215, USA
Received 2026 January 16; revised 2026 April 21; accepted 2026 May 5; published 2026 June 12

Abstract

ATLAS (Asteroid Terrestrial Last Alert System) is a time-domain survey using four telescopes, covering the entire sky. It has observed 8378 spectroscopically confirmed Type Ia supernovae (SNe Ia), with thousands of cosmology-grade light curves (to be released as TITAN DR1). To prepare this massive, low-redshift dataset for cosmology, we evaluate and cross-calibrate ATLAS forced photometry using tertiary stars from the DES (Dark Energy Survey) Y6 release. The 5000 deg^2 DES footprint overlaps regions both in and out of the PS1 (Pan-STARRS DR1) footprint, allowing tests of the primary calibrator for the ATLAS Refcat2 catalog. Initial offsets are at the ∼40 mmag scale. To improve this, we determine Δ zero-point offsets for two cases: (1) pixel-to-pixel offsets within individual CCDs (reduced from ∼8 to ∼4 mmag rms) and (2) chip-to-chip offsets across the nine CCDs and filters (reduced from ∼17 to ∼3 mmag rms). We also identify the largest systematic uncertainty as a transmission-function color dependence, requiring shifts in the assumed ATLAS filters at the ∼30 mmag level if uncorrected. We validate our calibration using (a) CALSPEC standards, (b) an independent tertiary catalog, and (c) distance moduli of cross-matched SNe Ia, all showing improved consistency. Overall, we estimate combined calibration-related systematics at the ∼5–10 mmag level, supporting competitive cosmological constraints with the TITAN SN Ia dataset.

Unified Astronomy Thesaurus concepts: Type Ia supernovae (1728); Cosmology (343); Hubble diagram (759); Tertiary stars (1691); Optical astronomy (1776); Transient sources (1851); Broad band photometry (184)

1. Introduction

Type Ia supernovae (SNe Ia), thermonuclear explosions of white dwarf stars, are one of the most successful standardizable candles thanks to their known luminosity–color–duration relationship (M. M. Phillips 1993; M. Hamuy et al. 1996; R. Tripp 1998). The small scatter in the post-standardization luminosity makes SNe Ia an excellent distance indicator for cosmology (e.g., A. V. Filippenko 2005). The state-of-the-art measurements of cosmological parameters, including the equation of state for dark energy (e.g., DESI Collaboration et al. 2025), use a compilation of SNe Ia samples that cover a wide range of redshifts, such as DESY5 (B. O. Sánchez et al. 2024), Pantheon+ (D. Brout et al. 2022; D. Scolnic et al. 2022), and UNION3 (D. Rubin et al. 2025).

A commonality among these datasets is that they combine low-redshift ($z \lesssim 0.1$) and high-redshift ($z \lesssim 1$) surveys. All SNe Ia datasets used in DESI Collaboration et al. (2025), DES (1500 high-z SNe Ia), UNION3 (containing more than 2000 high-z SNe Ia), and Pantheon+ (1550 high-z SNe Ia) take advantage of a common set of historical low-z datasets, which add up to ∼200 SNe Ia, (e.g., CfA1; A. G. Riess et al. 1999, CfA2; S. Jha et al. 2006, CfA3-Keplercam; M. Hicken et al. 2009a, CfA3-4Shooter; M. Hicken et al. 2009b, CfA4p1, CfA4p2; M. Hicken et al. 2012, CSP DR3; K. Krisciunas et al. 2017, LOSS1; M. Ganeshalingam et al. 2010, LOSS2; B. E. Stahl et al. 2019, SOUSA; P. J. Brown et al. 2014, Foundation; R. J. Foley et al. 2018a, CNIa0.02; P. Chen et al. 2022). Current constraints on cosmology rely on these historical low-z SN Ia datasets to point to interesting new physics (e.g., S. S. Boruah et al. 2020; D. Brout et al. 2022a; A. G. Riess et al. 2022; D. C. T. M. C. Abbott et al. 2024; M. Vincenzi et al. 2024; DESI Collaboration et al. 2025; X. T. Tang et al. 2025). This reliance on existing low-z datasets is problematic, because: (1) the number of low-z SNe Ia remains relatively constant whereas high-z datasets are growing rapidly with dedicated surveys, and (2) all analyses rely on this set of supernovae used not only for constraining nearby distances but also for training the underlying SN Ia model; this means that all cosmological analyses are inherently correlated. These will continue to be challenged for harnessing the full potential of upcoming flagship high-z surveys, such as

LSST (R. J. Foley et al. 2018b) and NASA Roman (R. E. Sanderson et al. 2024). This necessitates a renewed focus on the collection and analysis of precision low-z datasets, collected over many years.

While high-z SN Ia samples are expanding rapidly, the collection of a larger and less biased low-z SNe Ia poses a challenge. The volumetric SN Ia rate of $\sim 2 \times 10^{-5}$ SNe Ia yr^{-1} Mpc^{-3} corresponds to roughly one SN Ia per galaxy per century (B. Dilday et al. 2010). Even surveying the full sky, this yields only on the order of hundreds of SNe Ia per year within $z \sim 0.1$. Consequently, building a high-quality, spectroscopically confirmed low-z sample is inherently time-limited and requires continuous, nearly all-sky monitoring over many years. Upcoming surveys such as LSST will discover vast numbers of high-z SNe Ia, but LSST cannot rapidly discover low-z SNe Ia, since the limited nearby volume fixes the pace at which new low-z SNe Ia appear. In contrast to the explosive growth of high-z datasets, the buildup of precision low-z samples will remain a slow, volume-limited endeavor. In recent years, several new low-z SN Ia surveys have begun to expand this nearby sample, including the Zwicky Transient Facility (ZTF; M. Rigault et al. 2025), the Young Supernova Experiment (YSE; P. D. Aleo et al. 2023), and DEBASS (M. Acevedo et al. 2025; N. F. Sherman et al. 2025). These programs have made important contributions by increasing discovery rates and providing well-sampled light curves over limited sky areas. Differences in survey strategy, footprint, and calibration approaches mean that no single program yet provides a uniform, all-sky, long-baseline, cosmology-ready low-z ($z < 0.1$) SN Ia datasets of greater than a few hundred.

The TITAN (The Type Ia supernova Trove from ATLAS in the Nearby Universe) SN Ia dataset that we present in this series of papers will provide a solution with several thousand at low-z. TITAN is a compilation of spectroscopically confirmed SNe Ia observed by the Asteroid Terrestrial-impact Last Alert System (ATLAS; J. L. Tonry et al. 2018). ATLAS, a NASA-funded all-sky survey, visits the whole sky every night with limited magnitudes at $m \sim 20$ mag, making it optimal for capturing low-z SNe Ia up to $z \lesssim 0.1$. The first data release of the TITAN dataset, containing 8378 light curves ($\sim$3000 cosmology grade with host-galaxy z) consists of four papers. The overview, SN Ia light curves, and the Hubble diagram are presented in Y. Murakami et al. (2026); the association of SNe Ia with their host galaxies, the compilation of redshifts, and the determination of galaxy properties is the subject of J. Tweddle et al. (2026, in preparation); and the simulation and the forward-modeling of observational bias is presented in J. Tweddle et al. (2026, in preparation). In this paper, we externally validate the ATLAS calibration, motivate photometric corrections, and perform a preliminary calibration systematic assessment, in preparation for a future cosmological analysis.

The calibration of datasets, such as that performed in B. Popovic et al. (2025; hereafter Dovekie), consist of two steps: characterization of surveys' photometric systems (e.g., uniformity of the focal plane, temporal changes in transmission properties, linearity along wavelength and flux levels) and correction for each filter/detector configuration to a single reference photometric system. D. Scolnic et al. (2015; hereafter Supercal) calculate relative zero-point offsets using CALSPEC standard and a cross-validation with thousands of tertiary stars overlapping PS1 (Pan-STARRS DR1) and other telescope systems. This method was updated and improved upon in D. Brout et al. (2022b; hereafter Fragilistic) for Pantheon+, by allowing all surveys cross-calibrated simultaneously without fixing PS1, allowing for the production of a calibration covariance systematic error budget. Additionally, Fragilistic quantified the small variations of transmission functions and their impact on cosmology. Dovekie is the most recent iteration of this method, providing an open-source framework, an improved likelihood, and expanded sets of primary calibration stars with faint DA white dwarf stars. For calibration of the TITAN dataset in this work, we employ the same techniques in order to cross-check consistency of the existing ATLAS calibration with external datasets (HST Calspec, DA white dwarfs, Dark Energy Survey Y6 Wide Field Catalog).

ATLAS is a telescope network comprising four telescopes, two in the Northern Hemisphere in Hawaii (decl $\geqslant -50^{\circ}$), and two in the Southern Hemisphere in South Africa and Chile (decl. $\lesssim +40^{\circ}$) (J. L. Tonry et al. 2018).[12] An ATLAS camera system consists of a physical CCD device (all are STA-1600 devices with format 10,560 $\times$ 10,560 pixels) The northern telescopes underwent several changes to the camera configurations, which we document in Table 1. In particular, the Mauna Loa unit had four camera changes, while Haleakala has had the same CCD device throughout the survey. We define nine separate telescope and camera combinations over the decade since commissioning of the first unit on Haleakala, and we label each with a "chip ID." Each "chip" that we have defined may not be a unique CCD device. Rather, it is some combination of unique cryostat, detector, and controller. For cosmology, we treat each "chip ID" as an independent system. ATLAS primarily uses two broadband filters: ATLAS cyan ($4200 \lesssim \lambda_{\rm obs} \lesssim 6500$ Å) and ATLAS orange ($5600 \lesssim \lambda_{\rm obs} \lesssim 8200$ Å) (J. L. Tonry et al. 2018). With these two filters, we have 18 possible filter-camera configurations, e.g., chip 0—filter cyan, which we refer to as "chip 0c"). However for chips 0 and 2, the cyan filter was never used, which resulted in 16 filter-camera combination (see Table 1). In this work, we treat each combination as separate filters (similarly to CfA filters in Supercal).

The baseline ATLAS calibration, applied to every exposure in the default ATLAS data reduction pipeline, uses Refcat2, an all-sky tertiary star catalog in the PS1 system (J. L. Tonry et al. 2018). Refcat2 comprises photometry from eight distinct stellar surveys, primarily PS1, Gaia DR2, and APASS. The magnitude of each star is calculated as the average magnitude from each survey that observes it, opening up for potential mmag-level discontinuities across the sky. In this work, we use an independent, well-calibrated tertiary star catalog, that covers decl. ranges inside and outside PS1 to validate the baseline calibration with Refcat2. We select the DES Y6 tertiary star catalog (E. Rykoff et al. 2023), which is known to have a photometric uniformity of $<$1.8 mmag and whose absolute flux is known at the 1% level, making it an excellent candidate for a relative calibration. The footprint of 5000 deg^2 also provides a wide range of stellar photometry (with over 17

[12] ATLAS now has a fifth unit in Tenerife (ATLAS-TEIDE) that is operating as part of the survey. This is a different modular design constructed of 16 Celestron RSA 11 telescopes with a CMOS camera (J. Licandro et al. 2023). We do not use ATLAS-TEIDE data in any of the TITAN papers.

Table 1
Detector Configurations

Chip ID	Site	CCD Nickname	Cryostat	Serial Number	MJD_{min}	MJD_{max}
0	01a	fuzzy	gold	STA1600LN-SN 20526	57800	58715
1	01a	freckles	gold	STA1600LN-SN 25856	58719	59465
2	01a	fuzzy	green	STA1600LN-SN 20526	59466	59830
3	01a	wormy	magenta	STA1600LN-SN 31147	59830	⋯
4	02a	alien	red	STA1600LN-SN 19002	57800	58717
5	02a	alien	red	STA1600LN-SN 19002	58718	59519
6	02a	alien	red	STA1600LN-SN 19002	59522	⋯
7	03a	cruddy	blue	STA1600LN-SN 30634	59561	⋯
8	04a	freckles	gold	STA1600LN-SN 25856	59605	⋯

Note. The Site corresponds to telescopes as follows: Mauna Loa (MLO) = 01a, Haleakala (HKO) = 02a, South Africa (STH) = 03a, Chile El Sauce (CHL) = 04a. The chip ID represents the chip number that we use in this paper to define the combinations and date ranges. The CCD nickname and cryostat color are for ease of remembering the hardware and the formal serial numbers of the devices are listed to confirm the chip provenance. Note that chips 4, 5, and 6 are all the same configuration, on the same telescope, and allow us to examine the stability of the ATLAS detectors over time. Additionally, chip 8 is physically the same as chip 1 and was moved from MLO to CHL.

Table 2
Brief Descriptions of Each Tertiary Star Dataset Constructed, and Use Case in This Paper

Tertiary Star Catalog Name	Description	Use Case
Color-blind Sample	Baseline sample of stars common to DES and Refcat2	E.g.: Figures 1, 5, 6, 11
Blue Sample	Only blue ($g - i \leqslant 0.2$) stars common to DES and Refcat2	E.g.: Figures 1, 5, 6, 11
Non-refcat Sample	Random color and position sample in DES not in Refcat2	Used as validation in, e.g.: Figure 9

Note. See Section 2.1 for further details about the contents of this table.

million observed stars) facilitating cross-comparison, which is needed given the all sky nature of ATLAS.

We present the data used in this work, including ATLAS, DES, and synthetic photometry in Section 2. In Section 3, we quantify and discuss two levels of calibration (intra-chip and inter-chip) needed to prepare TITAN for cosmology. In Section 4 we demonstrate the tests used to show a validation of our calibration. We compare the resulting SN Ia luminosities with other modern low-z datasets in Section 5. We discuss the implications of our findings and their impact on cosmology in Section 6, followed by our concluding results in Section 7.

2. Data Preparation

2.1. Tertiary Star Samples

For this paper, we build three distinct tertiary star catalogs: "color-blind" sample, "blue" sample, and "non-refcat" sample (see Table 2). First, we construct a baseline sample of stars that are common to both Refcat2 and the DES Y6 catalog (K. Bechtol et al. 2026), with the natural Milky Way color distribution of stars. This sample is referred to hereafter as the "color-blind" sample. The color-blind sample has intrinsically few stars with $g - i$ color < 0.2, with most stars in the red ($g - i$ color > 0.2). Second, a catalog is constructed for only blue stellar colors (DES $g - i$ color $\leqslant 0.2$) from common Refcat2 and DES Y6 stars. This sample is referred to hereafter as the "blue" sample. We use this blue sample in our calibration because the SNe Ia primarily exist in this color range, and it enables us to create a uniform in color, total star catalog, for calibration (following D. Brout et al. 2019). We then re-sample our "blue" and "color-blind" catalogs to produce a tertiary star dataset that is uniformly distributed across the color range. This re-sampling is important because we measure the slope of our observed—synthetic data residual as a function of color for these stars. Having an even distribution of stars across the entire color range is important to avoid bias or not account for slope at a certain color. Third, we build a baseline sample of randomly distributed stars in sky position and color, from DES Y6 that are *not* found in the Refcat2 catalog. These stars are functionally similar to SNe Ia, an object whose color and brightness is not used in any part of ATLAS calibration (including initial Refcat2 zero-point calibration). This sample is referred to hereafter as the "non-Refcat2" catalog. For all samples, we apply cuts on the ATLAS data as recommended by the ATLAS team in J. L. Tonry et al. (2018) before analysis. We also apply cuts on ATLAS observations with excessively large errors ($\sigma_F \geqslant 2000\,\mu$Jy) or χ^2 above 5, and retain only stars with DES r-band magnitudes in the range $17 \leqslant r_{\rm DES} \leqslant 19$ mag. Figure 1 shows the locations of the stellar samples used. This figure only includes stars that pass cuts and are used in calibration (∼60,000).

Another aspect considered in the creation of our tertiary star samples is how ATLAS photometry is represented within Refcat2. Because ATLAS photometry is calibrated to the Refcat2 catalog, the surveys contributing to a given Refcat2 magnitude are important. We examine this effect in detail in Section 2.6. The primary result of this analysis is that stars with Refcat2 magnitudes derived solely from Gaia measurements exhibit significant systematic offsets relative to PS1. To avoid introducing this bias into the ATLAS calibration, we remove all calibration stars that are observed only by the Gaia survey in Refcat2.

2.2. ATLAS Forced Photometry

We take our three catalogs and obtain photometric measurements in ATLAS observations by performing the standard forced photometry routine (tphot; S. Sonnett et al. 2013). tphot is a custom point-spread function (PSF) fitting routine: it produces flux measurements based on the difference images of ATLAS forced photometry. We used tphot in forced mode and forced PSF fitting at their known positions. We worked with ATLAS infrastructure to ensure epoch photometry and data reduction with the same server pipeline that photometry and data reduction are done for the purposes of difference imaging for the SNe. This used the same software routines as available on the publicly available ATLAS forced photometry server (K. W. Smith et al. 2020; L. Shingles et al. 2021).[13] There is no proper motion involved in these requests. Instead, we apply an outlier rejection system and calculate stellar medians instead of means throughout our analysis. With enough sample size, we should be able to ignore stars with large proper motion and have enough sample remaining.

2.3. DES Photometry

The DES Y6 survey (E. Rykoff et al. 2023) is an incredibly robust (<2mmag relative uniformity over the survey region) and well-measured survey, covering a large 5000 deg^2 portion of the sky. Most of the 17 million stars contained within DES Y6 have i-band magnitude: $16 < i < 21$. The survey uses a modification of forward global calibration method (FGCM) from D. L. Burke et al. (2017) to remove positional discrepancies across the DECam CCD.

The absolute calibration is done with the Hubble Space Telescope (HST) CALSPEC standard star C26202 as specified by E. Rykoff et al. (2023). Including systematic uncertainties, DES photometry is calibrated to C26202 with an accuracy of approximately 1% in flux.

2.4. Synthetic Data

We generate synthetic ATLAS and DES photometry with NGSL templates (M. Koleva & A. Vazdekis 2012) and CALSPEC standard stars. We take transmission functions for ATLAS from J. L. Tonry et al. (2018). We do this by fitting a spectrum of a CALSPEC or NGSL star, to our filter functions wavelength grid. We then integrate this spectrum flux in the photon count space (as opposed to the energy space), and convert this to AB magnitude at the photon pivot wavelength, where AB mag has to be defined in the frequency space. The photo pivot wavelength is a filter-dependent wavelength that allows for direct wavelength frequency conversion of flux densities. In order to do this at a large scale, we modified the code from B. Popovic et al. (2025) to include the ATLAS filter functions. This enables us to produce synthetic stellar photometry for all of our filters, and quickly apply wavelength shifts to the filter functions. Our method also allows us to adjust or shift the bandpass wavelength if we find discrepancies.

2.5. ATLAS CCD-filter System

ATLAS's four telescopes, nine CCDs, and two filters (orange and cyan), result in 18 unique CCD-filter configurations. CCD Chips 0 and 2 never took data in the cyan band, leaving 16 total CCD-filter configurations. The four telescopes that comprise ATLAS began operating about a decade ago with the first northern telescope starting operation in 2015 June (HKO), the second in 2017 February (LMO), and the two southern telescopes starting in 2021. We chose to start the TITAN data sampling, and the calibration data, in early 2017 (MJD = 57800), at a time when the northern ATLAS units had settled down to a stable operating mode and hardware configuration. Figure 2 shows the transmission curves of each ATLAS and DES filter as a function of wavelength, with a reference CALSPEC stellar spectrum. We observe that ATLAS's coverage approximately lines up with the DES g, r, and i bands.

Another key note is that the quantum efficiency (QE) is not uniform between the CCDs used in the two northern telescopes (Table 1 shows the changes in CCDs). It is largely uniform until $\lambda = 6500$ Å, where there is deviation over the rest of the wavelength we use. We do not attribute substantial effects in our calibration with QE. See Figure 3 in J. L. Tonry et al. (2018) for additional details about QE in ATLAS.

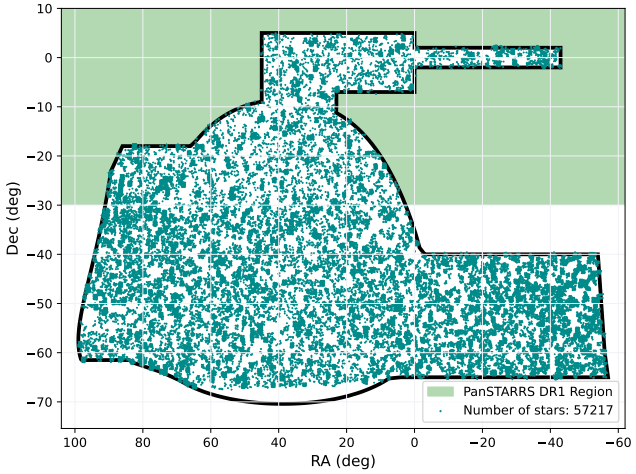

Figure 1. Each individual star by R.A. and decl. used in analysis. The DES footprint is overplotted here along with the Pan-STARRS region. Note that the southern telescopes take over slightly below the PS1 region at a decl. of −50°. Stars were chosen in 1 deg^2 chunks randomly distributed throughout the DES footprint. There are 500 chunks each containing roughly 200 stars in our "color-blind" sample, and about 50 stars over 500 chunks in our "blue" sample. In total, there are roughly 125,000 stars with full ATLAS history light curves collected, although this number is reduced after cuts described in Section 2.

2.6. Refcat2 Catalog Validation

For each image we collect from ATLAS, there is a zero-point calculated using stars from the Refcat2 catalog. This catalog is a combination of many different surveys to facilitate all-sky coverage for ATLAS. The primary surveys involved here are PS1 (H. A. Flewelling et al. 2020) and Gaia (Gaia Collaboration et al. 2018), with GAIA, APASS DR9 (A. A. Henden et al. 2016), and Skymapper DR1 (C. Wolf et al. 2018) in the south (J. L. Tonry et al. 2018).

First, we aim to validate that no single survey from Refcat2 is providing chromatic or skewed data, thus biasing ATLAS photometry. The Refcat2 catalog combines every survey that measures a star's magnitude and averages them together. There is no clean way to determine a single survey's contribution to the Refcat2 magnitude value when multiple surveys observe a star. Thus, to conduct this validation, we

[13] https://fallingstar-data.com/forcedphot/

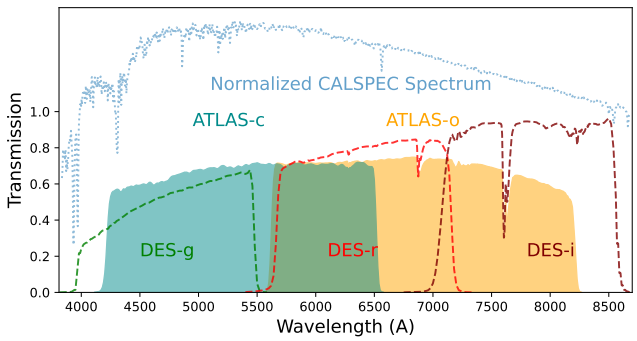

Figure 2. Transmission vs. wavelength for ATLAS orange and cyan bands. The DES *g*, *r*, and *i* bands used for cross-calibration are shown for reference. Transmission throughput data comes from the SVO2 Filter Profile Service. Also overplotted is HST CALSPEC synthetic star hd009051 used in our calibration. The CALSPEC star's flux density is scaled up arbitrarily, to be visible on the same scale as the filter functions.

examine Refcat2 stars that (1) only have contribution from one survey, or (2) are specifically missing contribution from one survey. This allows us to isolate effects that might occur from each survey individually. Our primary finding is that stars only measured by Gaia are skewed substantially off the main PS1 survey (above decl. of −40). One explanation of this could be the transformation functions are not perfectly fit at color $g - i < 0$, since this is outside the color range of a typical Milky Way star. To avoid this potential bias in ATLAS photometry, we filter out all calibration stars that only have observations by the Gaia survey. To be clear, this is not a statement about PS1 and Gaia generally, but only for their calibration within the Refcat2 catalog.

Other than the discrepancy with Gaia, the rest of the surveys match well with the trend of PS1, including the other surveys in the south where PS1 data does not exist. This is facilitated by the overlap from the highly uniform DES Y6 catalog facilitating comparison. We remove stars that only have Gaia measurements in Refcat2 from our calibration.

3. Analysis

We break our calibration down into two primary components. First, we have the intra-chip calibration, where we have examined CCDs of each telescope repeatedly to determine trends within the CCD at the binned (tens of pixels) pixel level that can be corrected and facilitate better nightly precision. This provides a coarse *x*–*y* positional dependence measurement. Second, is inter-chip calibration. We examine trends across all filter-chip combinations to produce a median Δ zero-point (ΔZP) offset for each individual chip-filter. This portion also includes shifting any filters in wavelength to correct for chromatic effects. We conduct this filter shift in a phenomenological manor, focusing primarily on optimal calibration for SN Ia cosmology.

3.1. Intra-chip Variation

The untargeted, all-sky survey pattern by ATLAS creates a dither pattern around each star's coordinate. This pattern provides an insight into the sensitivity function's possible variations within each CCD, as tertiary standard stars are measured at many different CCD coordinates and across the focal plane.

ATLAS CCDs have 10560 x 10560 pixels (STS—1600 model), and each image is read out in 1 × 1 binning by default. Median seeing is 3.″7–5.″6, which span 2–3 pixels at FWHM, with each pixel containing 1.″86. The `tphot` forced photometry routine reports the CCD coordinates (*x*,*y*) that correspond to the requested sky coordinates for the forced photometry. We use this information to construct the coordinate-dependent zero-point offset map within each chip, with the initial per frame Refcat2 zero-point already calibration applied.

The procedure is as follows: for any given star, we have multiple observations across different *x*, *y* coordinates in multiple CCDs. Then, for any star with data in a given CCD, we take the median of all magnitude values, and subtract that from each individual observation magnitude value. This creates a coordinate-dependent offset of one star mapped across all chips. We then repeat for every star producing a heatmap of the coordinate based offset within a CCD. Figure 3 shows the results of this process. Because we are looking for a coordinate dependence, we subtract out the median offset from each chip, to make net offset 0 if there is no coordinate dependence. As shown in G. M. Bernstein et al. (2017), we are ignoring edge effects on all of the chips, as those are notoriously unreliable across CCDs; thus, they are cut out, at the 50 pixel scale, before correcting.

Figure 3 shows that chips 0–7 have no particularly concerning patterns, i.e., variation at the 50 pixel level. We can see some distinct patterns on the 1 mmag level. Since these are different filters and, thus, data in one filter is independent of data in another, this is a strong validation that these patterns (and thus those more significant like chip 8o) are physical results, and not a product of our data processing.

Chip 8o has a significant vignetting pattern with brighter magnitude residuals toward the right side and slightly at the top of the chip. Figure 4 also shows a scatter plot of the *x*- and *y*-axes of chip 7 on the top plots, and the same plot for chip 8 on the bottom plots. Clearly visible here is the trend in the *x*-axis of the chip toward brighter observations on the right. A significant observation from Figure 4 is that this vignetting pattern, producing brighter observations in chip 8o, only exists in the orange band.

We account for this vignetting pattern in our correction model. We create the correction model by binning the pixels of each chip into 50 pix bins. We use our calculated "optimal smoothing radius" of 540 pixels (Appendix C), to convolve our 2D arrays using python's `Gaussian2DKernel`. This convolution then gets remapped to the entire 10,560 x 10,560 pixel space to produce a complete correction map for one chip. Our model applies unique corrections to each chip and each filter separately (16 total correction maps). These maps are then combined sequentially and applied to our calibration.

3.2. Inter-chip Variation

The inter-chip offset is described as the vertical shift between the observed ATLAS–DES transformation function and the synthetic transformation function in Figure 5 for each chip. It can be defined for the *i*th star as:

$$\Delta_{i,x1,x2,y1,y2} = m_{i,y1}^{\mathrm{ATLAS}} - m_{i,y2}^{\mathrm{DES}} - f_{y1\rightarrow y2}^{\mathrm{synth}}\left(m_{i,x1}^{\mathrm{DES}} - m_{i,x2}^{\mathrm{DES}}\right). \quad (1)$$

We fit a single offset value to an ATLAS filter so that the empirical ATLAS–DES filter transformation matches the synthetic prediction. See Appendix A for details on the

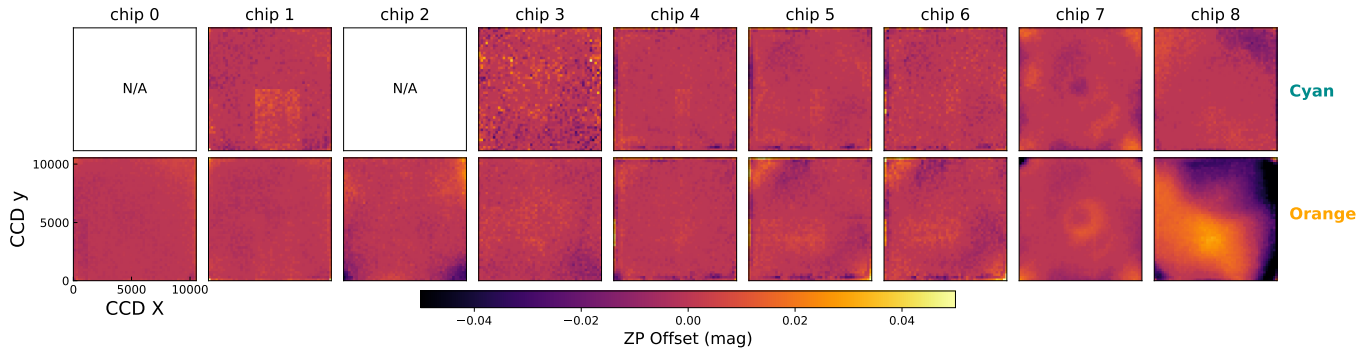

Figure 3. The magnitude residual within each chip (zero median). Median binning applied for visualization and calibration (50 pixel bins). The heat maps have median residuals of each chip subtracted out. This facilitates characterization of coarse x–y positional variation measurements at the tens-of-pixel level. See Section 3.1 for details on heatmap construction. Note the dramatic variations for chip 8o. No inter-chip or wave-shift correction is applied.

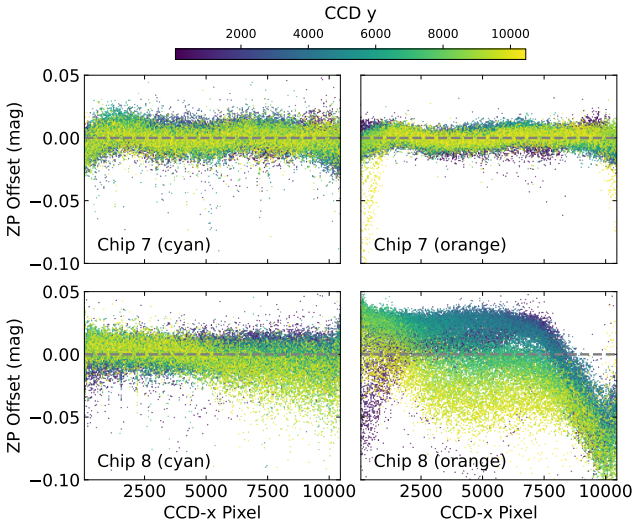

Figure 4. Collapsed 1D views of two chips (7, 8) from Figure 3 in orange and cyan bands. The pixel offsets in magnitude are shown on the y-axis, and the x-axis shows the x pixels corresponding to Figure 3. This shows the significant nonuniformity of chip 8o as a function of the x pixel. Note how in cyan, while variations are larger for chip 8 compared to chip 7, there are no significant deviations from uniformity. Chip 7 is representative of a more typical chip used in this analysis, and chip 8 is highlighted as an area for future improvement and ongoing work.

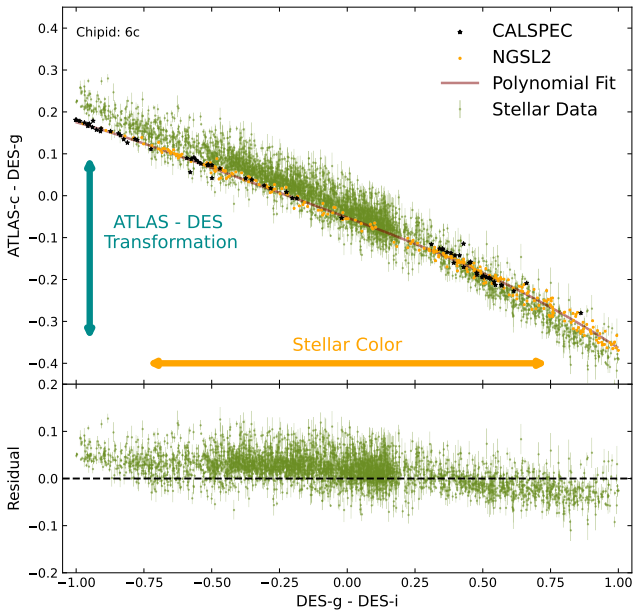

Figure 5. ATLAS–DES transformation (ATLAS-c - DES-g) vs. DES color $g - i$ for ATLAS chip 6c. Real stellar data from ATLAS server and DES Y6 is shown in green. Both NGSL and HST CALSPEC synthetic stellar photometry (orange, black) are overplotted. A fifth-order polynomial fit to the synthetic NGSL data (brown) is shown. The bottom plot is the real data residual to the polynomial fit. The bottom residual plot demonstrates a residual chromatic slope that must be accounted for. The net vertical shift of the green points relative to the trend line shows the inter-chip offset. The actual calculation of these offsets is substantially more complex than what is shown here, and the likelihood and fitting process are described in detail in Appendix A. This inter-chip correction is applied *after* accounting for intra-chip variation.

likelihood function used to define this transformation. The residual plot on the bottom of Figure 5 shows the value of the vertical shift as a function of DES color. The residual is calculated as the y-axis difference between the real data at that color and the value of a polynomial fit to the synthetic NGSL2 photometry. The synthetic polynomial is a fifth-order approximation of the synthetic data using Python's `Polynomial.fit`.

We expect that this residual is a flat line centered away from 0. The amount this line is offset from 0 would be the zero-point offset of this chip-filter combination (there is a collapsed likelihood function used here to generate this, but it is still the result of this residual). This is the zero-point offset because the synthetic data uses CALSPEC stars, which have the absolute flux of our filter function. Figure 6 shows the results of this zero-point offset: these are the values that are applied to each respective chip during the inter-chip correction.

Notably, there is a $g - i$–color-dependent trend in the residuals (the bottom plot of Figure 5 shows the most egregious case; most chips are substantially better). Considering that this is the residual of observed photometry from the synthetic photometry, the presence of a slope implies that our filter transmission functions used for the synthetic photometry differ from each telescope-detector-filter combinations' actual throughput. Figure 7 shows this chromatic effect slope across all chips. Note the systematic chromatic effect in the cyan band versus the minimal effect in orange. Also note that because chips 4, 5, and 6 are all the same camera setup over time, we can use this to observe that the chromatism worsens with time even within a single chip. This is not an unusual observation: previous cosmology-grade calibrations of SNe Ia catalogs, such as D. Brout et al. (2022a) and B. Popovic et al. (2025) have identified chromatic slopes using a similar method. Unless a careful, laboratory-level re-measurement of the system throughput can be performed, these slopes are

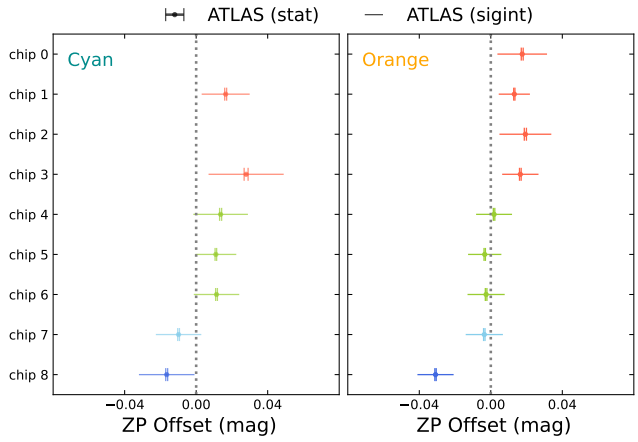

Figure 6. This figure summarizes the inter-chip zero-point corrections applied for each chip. These offsets are the zero-point shift of the real data from the synthetic data in ATLAS–DES transformation vs. color, as demonstrated in Figure 5 and calculated following Appendix A. Two error bars are displayed: (1) the smaller errors represent the statistical ("stat") uncertainty resulting from the ATLAS data, and (2) the larger errors represent the dispersion of the data ("sigint").

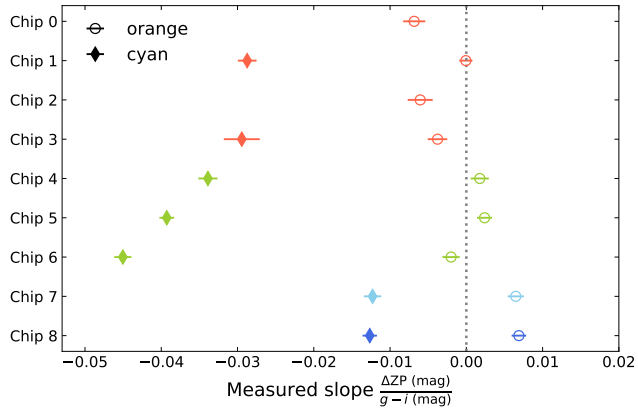

Figure 7. The measured slopes (ΔZP) of the residuals to polynomial fits (illustrated for chip 6 at the bottom of Figure 5) for each chip (*y*-axis). An example of the slope measured can be seen visually in the bottom panel of Figure 5. Points are colored according to which telescope each chip corresponds to in the order presented in Table 1. The larger the slope value, the larger the wave shift we apply; thus, this plot indicates the significance of the shift. Actual shift values presented in Table 3.

typically corrected by applying modifications to each filter's transmission function. Figure 8 demonstrates the color-dependent (chromatic) effect of such modifications: two distinct methods (wavelength shift and filter tilt; see B. Popovic et al. 2025 for review) produce a nearly identical color-dependent change in the predicted magnitudes. For consistency with the literature and simplicity, we choose to employ the wavelength-shift method. A correct choice of wavelength shift can match the measured slope in the tertiary stars, effectively mitigating the chromatic effect during the light-curve fitting of the cosmological SNe Ia samples.

The measured slopes and, therefore, implied filter shifts are most pronounced for cyan, where we find each chip should be shifted by 50–100 Å in the same direction. Although this initially sounds substantial, given how broad the ATLAS filter bands are, this is comparable to shifting a DES or PS1 band by 25–50 Å, which has been shown to be necessary in some cases (e.g., PS1-*g*; D. Scolnic et al. 2015). While the exact cause of the observed chromatic effect is unknown (e.g., change in

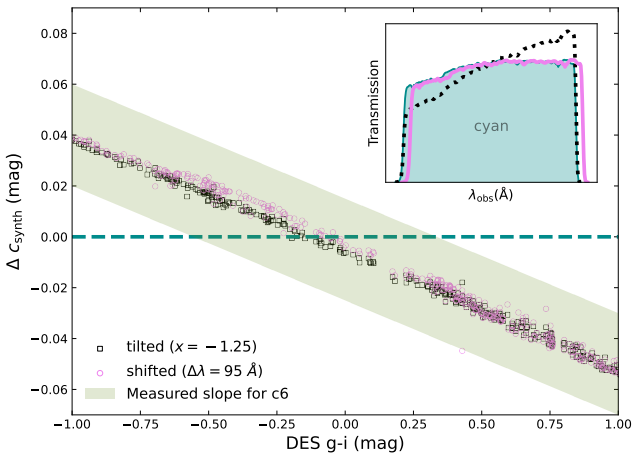

Figure 8. The *y*-axis is the synthetic magnitude of cyan band with no shift minus the magnitude with a wavelength shift. The *x*-axis is DES $g - i$ color. Both 95 Å. coherent shift (pink) and a tilted throughput with $X = -1.25$ (black; see Equation (8) in B. Popovic et al. 2025 for definition) are shown for comparison. The green shaded region shows the observed tilt for chip 6c; the most extreme case shown in Figure 5. The subplot in the top-right corner shows the original, shifted, and tilted transmission functions.

quantum efficiency, filter degrading, calibration issue), our phenomenological approach is efficient at removing the observed chromatic effect, and is backed up in the literature as a viable solution for cosmology. Furthermore, in Section 4.2, we will demonstrate the validity of these cyan shifts on the independent CALSPEC spectrophotometry.

4. TITAN Calibration Validations and Tests

We validate our calibration in three ways. Against an independent tertiary star catalog ("non-Refcat2" catalog from Section 2.1), using HST CALSPEC primary calibrators and DA white dwarfs, and analysis of coordinate dependence of the tertiary star residuals before and after correction.

4.1. Validation with Independent Tertiary Catalog

We first validate using tertiary stars that are not contained in the Refcat2 catalog and, therefore, are not used in our calibration solution. These stars are identified in the DES Y6 catalog for which ATLAS forced photometry is obtained as outlined in Section 2.2 (this is what is referred to as the "non-Refcat2" catalog in Section 2). This provides an independent photometric dataset for validation. From the perspective of ATLAS, these "non-Refcat2" stars behave functionally the same as SNe Ia: a point-source object that is not included in zero-point calibration of each image. Figure 9 displays the effect our calibration has on these validation stars. Additionally, the error bars on these points represent the percentile range (16th percentile to 84th percentile) of the median value offset of a chip.

Figure 9 shows the results for the "non-Refcat2" stars before and after our calibration solution. First, we find that the scatter in stars (16th percentile to 84th percentile error bars) is reduced, especially in the cyan band. Second, after correction, all of zero-point offsets relative to DES are near zero. Note that all of the stellar scatter for chips 4c, 5c, and 6c is reduced substantially with correction, which is the result of accounting for the chromatic slopes.

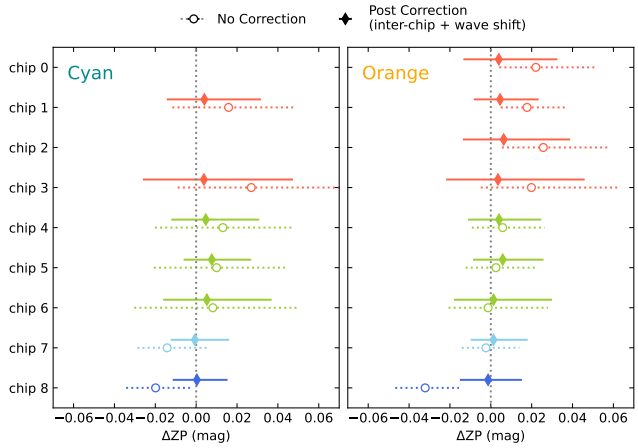

Figure 9. Δzero-point offset in magnitude between observed and synthetic photometry (the same definition as in Figure 6) for a validation sample of stars that are independent of Refcat2, before and after our calibration correction. The ΔZP value is the offset between chips and is corrected by the inter-chip correction. The error on the values is the result of a projection of the residuals from Figure 5 into the ΔZP offset space, representing the scatter in residual. This error is dominated by the chromatic slope displayed in Figure 7.

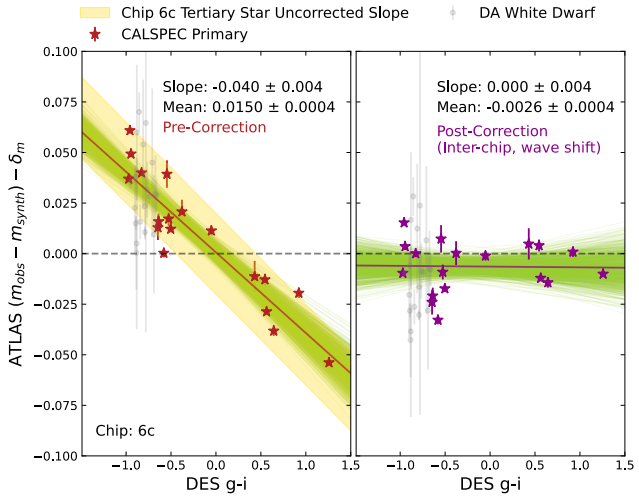

Figure 10. Synthetic minus observed residuals of several CALSPEC stars, including C26202, and DAWD, for ATLAS cyan band (chip 6c) vs. DES color in $g - i$. This is nearly identical to the bottem panel of Figure 5 but now demonstrating the impact of our calibration corrections. The many green lines represent random slope draws from the likelihood fit that account for covariance to show a range of possible fitted slopes and uncertainty. The solid lines are the best-fit slopes. We note that values for all chips are reported in Table 4.

4.2. Validation with HST CALSPEC and DA White Dwarf Reference Stars

The second validation method we employ is using primary, and secondary stars to reproduce Figure 9. We use a combined dataset of spectroscopic flux-calibrated standards, HST CALSPEC (R. C. Bohlin et al. 2014), and DA-type faint White Dwarfs (DAWDs; B. M. Boyd et al. 2025), to further validate our results and quantify systematic uncertainties. These spectroscopic standards, observed by HST/STIS with an absolute calibration to physical units, provide a direct comparison of synthetic and observed spectra without the need of deriving the synthetic color–color transformation (Equation (A1)). This independence, along with the broadly accepted use of the CALSPEC stars for photometric calibration, makes them an excellent probe to test the possible systematics in the post-correction photometry of the TITAN dataset.

In addition to enabling an independent check of our tertiary star-based methods, the use of CALSPEC stars is relevant to the original calibrations of DES and ATLAS. DES uses a single primary calibrating star's spectra for its calibration to the absolute AB magnitude system, HST CALSPEC C26202. DES claims that, including systematic errors, the absolute flux is known at approximately the 1% level. DES generates these synthetic magnitudes by integrating the official DES passband throughputs with one of standard spectra for C26202 from the HST CalSpec database (R. C. Bohlin et al. 2014). PS1, on the other hand, does not use a single CALSPEC star for its absolute calibration; instead, they rely on Ubercal from E. F. Schlafly et al. (2012) for the initial zero-point calibration, which is then tied to the physical units using multiple CALSPEC standards (E. A. Magnier et al. 2020).

In Figure 10, we present the measured offset between synthetic and ATLAS-observed photometry of chip c6 using CALSPEC and DAWD stars. An additional mmag-level offset $\delta_m = m^{\rm DES}_{\rm C26202} - m^{\rm synth}_{\rm C26202}$ is subtracted to account for the difference between the DES photometry of their absolute-scale calibrator, C26202, and our synthetic photometry. This is possibly due to the small, numerical effect from the difference in subsampling along the wavelength axis. We calculate a slope and offset $\Delta{\rm ZP}_i = \bar{\mathcal{A}} \cdot (g - i)_i + \mathcal{B}$ (the purple line in Figure 10) in our post-correction residual. We use the values of the slope ($\bar{\mathcal{A}}$) and the intercept ($\mathcal{B}$) to quantify systematic uncertainties (Section 6.3).

We see in Figure 10 that our corrections improve the offset and chromatic effect. The mean is reduced from 0.015 pre-correction to −0.0026 post-correction. The chromatic slope is reduced from −0.0399 pre-correction to −0.0004 post-correction. This improvement in slope and offset is an independent validation of the methodology using tertiary star cross-calibration with DES. We show chip 6c as an excellent example validation of our filter-shift correction. We do not present any orange band data for primary calibrators in this plot, as orange band data already has a minimal slope, and corrections are extremely small (we find an uncorrected median slope of 0.004 in the orange band). We will discuss the resulting reduction of systematic uncertainty in Section 6.3.

4.3. Coordinate Dependence

When calibrating four independent telescopes, it is important to verify there is no residual coordinate dependence (due to the different physical locations of the telescopes). There are two main regions we might expect coordinate dependence: above/below −50° decl., where the northern telescopes cut off, and above/below −30° decl., where PS1 (the primary calibrating instrument of ATLAS Refcat2) cuts off.

In Figure 11 we can see, before our DES cross-calibration, there is a coordinate-dependent offset at the northern telescope cutoff (the bluer region below −50° decl.). We are able to remove this offset with our inter-chip corrections, as can be seen on the right side of the plot. Also apparent is a slightly less-defined discrepancy at a decl. of −45°, where the bore sights of the northern telescope pointing positions are set. Beyond this, we see no effect at the boundary of the PS1 region, implying that APASS and Skymapper in the south are

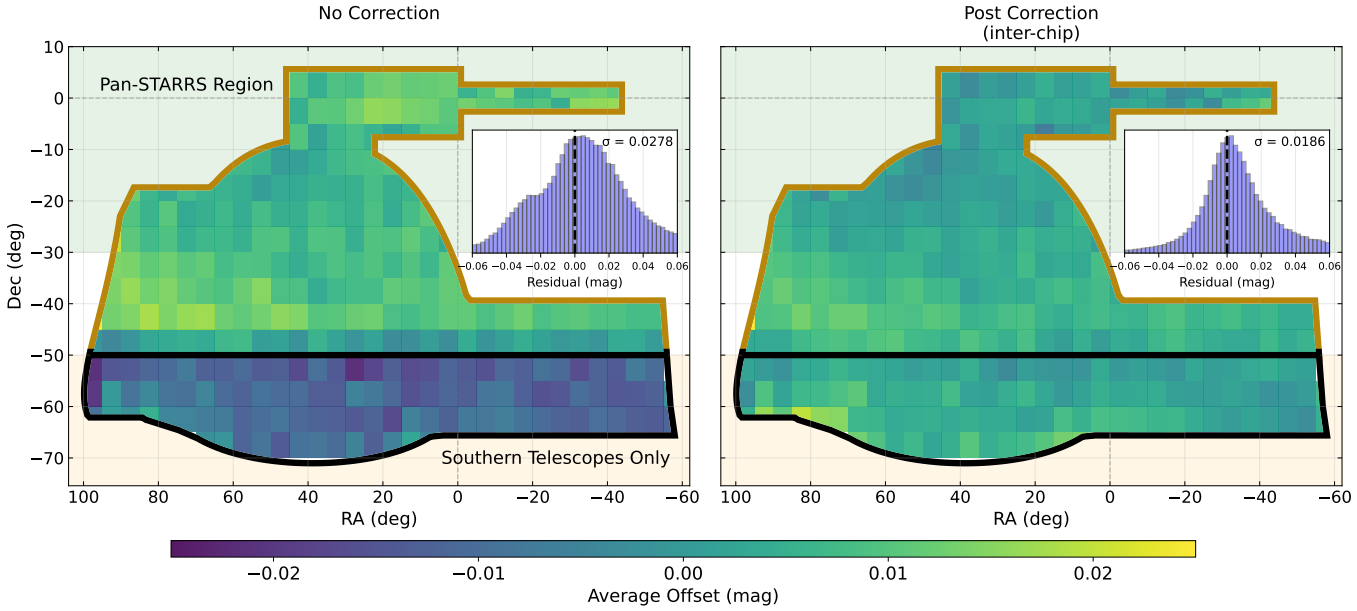

Figure 11. Heatmap of median offset as a function of spatial position before and after inter-chip corrections. After corrections, the spatial dependence and the standard deviation of the residuals improve. This is most noticeable around −50° decl. where the northern telescopes cut off. The histogram residuals between ATLAS and DES stars after corrections becomes substantially more Gaussian.

sufficient calibration catalogs. Therefore, the right side of Figure 11 shows that applying our inter-chip correction creates uniformity across the entire DES footprint, and specifically resolves the issues with the southern telescope calibration. In the histograms in Figure 11, we find the scatter between ATLAS and DES photometry after transformation reduces substantially after our correction (from 0.028 mag to 0.019 mag), and the histogram of all ATLAS–DES tertiary comparisons becomes more Gaussian.

5. Distances and Hubble Diagram Residuals

We apply the calibration defined in this work to the light curves of TITAN DR1 gold (Y. Murakami et al. 2026), hereafter DR1. In DR1, light curves are fit with the SALT3-DESY5 model using the SNANA package (R. Kessler et al. 2009). Our intra-chip, inter-chip, and wave-shift corrections are applied specifically during SALT3 fitting (see Figure 13 for details on the calibration application). This fit yields stretch (x_1), color (c), and B-band model magnitude (m_B), and the time of maximum (PKMJD) for each SN. Note that there is a cut on color error at $\sigma_c < 0.1$, for details and discussion on the light-curve fits and model residuals; see Y. Murakami et al. (2026).

We compare the fitted light-curve parameters (x_1, c) against the fits to the light curves of the same, cross-matched SN observed by external surveys (DEBASS, YSE, and ZTF). Additionally, we apply a simple standardization using the SALT2mu routine (J. Marriner et al. 2011), which finds an optimal set of coefficients for stretch–luminosity relation (α) and color–luminosity relation (β), as well as a few additional nuisance parameters. Using an arbitrary absolute magnitude M_B, this yields a standardized, distance modulus (solely for the purpose of one-on-one comparison):

$$\mu_{\text{test}} = m_B + \alpha \cdot x_1 - \beta \cdot c - M_B. \quad (2)$$

For the purpose of direct, one-to-one comparison of cross-matched SNe across surveys, neither bias correction nor the typical "mass step" is needed. We use the same set of (α, β) across all surveys.

Figure 12 shows a comparison between TITAN and the three other low-z surveys in stretch, color, and distance. We describe the data from additional surveys used in this comparison (ZTF, DEBASS, and YSE) and discuss the implications in the following sections.

5.1. ZTF

The second data release of ZTF SNe Ia sample contains 2667 spectroscopically confirmed Type Ia SN with matching redshifts in the low-z region ($z < 0.3$) that pass initial cosmology cuts (M. Rigault et al. 2025). We find 474 cross-matches with TITAN. This is one of the largest spectroscopically confirmed low-z supernova datasets to date. We compare to ZTF as the only other low-z sample with SNe counts on the same order of magnitude as TITAN. Note that ZTF claims to have not completed their calibration for cosmology due to an observed 'pocket effect' of flux-dependent PSF biases. The ZTF group also noted in L. Lacroix et al. (2025) that an offset in the DR2 magnitude values on the order of 0.09 mag is needed to correct the overestimated flux in ZTF DR2 (M. Rigault et al. 2025). A separate group, M. J. B. Newman et al. (2025), found ZTF to be too bright by 0.024mag in comparison with 28 SNe Ia in common from Las Cumbres Observatory (LCO) *gri* photometry.

5.2. DEBASS

DEBASS (Dark Energy Bedrock All Sky Supernova program) has collected the largest (> 500 SNe Ia) uniformly calibrated low-z dataset in the *southern sky* to date (N. F. Sherman et al. 2025). They have already released 77 spectroscopically confirmed SNe Ia that pass cosmology cuts

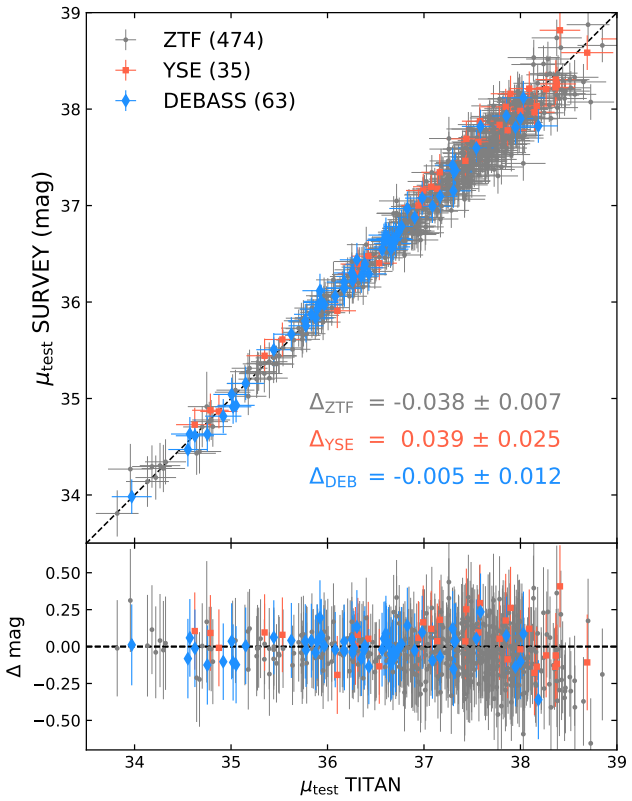

Figure 12. Fiducial distance moduli μ_{test} for SNe included in both TITAN DR1 and other modern low-z surveys. TITAN light curves are presented in the companion paper, Y. Murakami et al. (2026). Compared against ZTF DR2, DEBASS DR1, and YSE DR1. We use a conservative color error cut in TITAN SALT3 color, $\sigma_c \leqslant 0.1$, to minimize the known error-dependent bias (see Y. Murakami et al. 2026 for discussion). The measured offsets are consistent with zero for YSE and DEBASS. The significant offset between ZTF and TITAN is consistent with the known offset for ZTF reported in M. J. B. Newman et al. (2025).

in DR 0.5 (M. Acevedo et al. 2025). DEBASS operates in the southern sky with a similar redshift range as TITAN ($0.01 < z < 0.08$), and here, we utilize >400 SNe Ia in DEBASS DR1 (N. F. Sherman et al. 2026, in preparation), which results in 63 matches with TITAN cosmology-quality light curves. DEBASS claims high signal to noise, low Hubble residual scatter (0.1 mag) light curves, resulting in a reasonably strong constraint on the offset between ATLAS and DEBASS. This should enable excellent cross-matching of SNe Ia once DEBASS DR1 is released, and we can find hundreds of matches. Becasue DEBASS is calibrated to DES Y6, and, as demonstrated in this paper, ATLAS is now tied to DES Y6 as well, we do not use any offsets here.

5.3. YSE

YSE comprises data from ZTF and PS1, and contains 451 spectroscopically confirmed and cosmology-grade SN Ia light curves (P. D. Aleo et al. 2023). We find 35 cross-matches with TITAN. The YSE redshift range is generally higher than TITAN ($z < 0.5$), yet this still results in 35 matches with our TITAN low-z dataset. We use the PS1-Dovekie (B. Popovic et al. 2025) offsets relative to DES-Dovekie in order to place YSE on the DES Y6 system and to facilitate comparison with TITAN.

Table 3
Orange and Cyan Band Zero-point Offset Corrections and Wavelength Shifts for TITAN Calibration

Chip	Δm_{cyan} (mag)	$\Delta\lambda_{cyan}$ (Å)	Δm_{orange} (mag)	$\Delta\lambda_{orange}$ (Å)
0	…	…	+0.176 ± 0.0005	+22 ± 2.7
1	+0.017 ± 0.0005	+56 ± 1.4	+0.013 ± 0.0003	+5 ± 1.7
2	…	…	+0.019 ± 0.0006	+25 ± 3.1
3	+0.028 ± 0.0011	+57 ± 2.4	+0.017 ± 0.0005	+27 ± 2.8
4	+0.014 ± 0.0006	+67 ± 1.4	+0.002 ± 0.0004	−6 ± 2.1
5	+0.011 ± 0.0004	+78 ± 1.1	−0.003 ± 0.0004	−6 ± 1.9
6	+0.011 ± 0.0005	+87 ± 1.6	−0.003 ± 0.0004	+10 ± 2.4
7	−0.010 ± 0.0005	+28 ± 1.1	−0.004 ± 0.0004	−15 ± 1.8
8	−0.017 ± 0.0005	+28 ± 1.0	−0.031 ± 0.0004	−21 ± 1.8

Note. Zero-point offset corrections are in units of magnitude while wavelength shift is in units of Å. Note that both Δm and $\Delta\lambda$ need to be used as a set, as Δm is calculated as an offset from a synthetic photometry using the corresponding $\Delta\lambda$ for each chip.

5.4. Comparison of μ_{test} for Coincident SNe Ia

In Figure 12, the observed μ_{test} for coincident SNe Ia between TITAN and both DEBASS and YSE is found to be in agreement, with average offsets between the surveys of -0.005 ± 0.012 and $+0.039 \pm 0.025$, respectively. We do find, as expected, a significant offset for ZTF DR2 (-0.038 ± 0.007), suggesting that the ZTF DR2 photometry is bright relative to TITAN. While this ZTF DR2 offset is in agreement with the offset presented in M. J. B. Newman et al. (2025), we do not find strong evidence for an offset of ZTF DR2 at the 90mmag level, as presented in L. Lacroix et al. (2025). Overall, in comparison to the surveys that have been used in modern cosmology analyses (YSE/PS1 and DEBASS/DES), we find no direct evidence of systematics.

6. Discussion

6.1. Chromatic Effects

We identify a color-dependent calibration residual with an amplitude of ~0.005–0.045 mag over the $g - i$ range relevant for TITAN SNe Ia. The effect is most pronounced in the cyan filter, particularly for the sitecam 02a system (chips 4c, 5c, and 6c), as shown in Figure 7. For chips 4c, 5c, and 6c, there is a clear progression toward worsening color-dependence over time. Conversely, chips 7c and 8c, which are associated with the newer southern telescopes, have substantially smaller chromatic trends. This temporal and instrumental coherence points to an instrument-level effect. This could be explained plausibly by small mismatches between the assumed and true filter transmission functions, evolution of detector quantum efficiency, or wavelength-dependent throughput changes elsewhere in the optical system all of which could lead to color-dependent zero-point offsets. Resolving the physical cause of this chromatic effect will require further experimentation. The main thrust of the work presented here is that we are able to adequately correct this chromatic effect for cosmology by shifting the filter throughput in wavelength.

6.2. Intra-chip Correction for Use in Cosmology

The intra-chip corrections derived in this work are generally small and spatially smooth for all detector configurations, with the exception of chip 8 in the orange band (8o). Chip 8o exhibits a pronounced spatial structure, with a clear gradient toward the right side and upper portion of the detector. While we construct and apply a correction map for this chip and include it in preliminary distance measurements, the amplitude and coherence of this feature distinguish it from the lower-level intra-chip structure seen elsewhere in the focal plane.

Upon further investigation, we find no corresponding offset in the image-level zero-point solution nor a spatially coherent deviation in the DOPHOT-based stellar photometry, indicating that the effect arises downstream in the forced photometry process. In particular, the discrepancy appears only in the forced photometry, which utilizes a spatially variable PSF model. While this rules out a bug in the core ATLAS processing and implies peculiarities of the 8o PSF, the underlying cause is thus far unidentified.

Given this, chip 8o represents the dominant contributor to residual intra-chip uncertainty in the current TITAN calibration. We do not attempt to further absorb this effect through ad hoc error inflation. Instead, our preferred approach is to identify and correct the underlying cause of the forced photometry behavior prior to cosmological analyses. Our intra-chip correction is applied in this DR1 release, as it reflects the photometry exactly as produced by the current ATLAS pipeline used for cosmology-quality SN Ia light curves being released by TITAN. Any upstream changes to PSF handling would result in future releases that will supersede this work. In future cosmological analyses, we will evaluate the possible systematics due to the anomaly in chip 8o and the state of its potential resolution or lack thereof.

6.3. Systematic Uncertainty

In this paper we present preliminary estimates of systematic uncertainties due to calibration for future TITAN cosmology constraints. We define four sources of systematic uncertainty in this work, which are summarized in Table 5. The first is the systematic uncertainty on the intra-chip correction, resulting in a per-exposure magnitude error floor. This is calculated as: $\epsilon_{\rm intra} = \sigma(\mathcal{O} - \mathcal{M})$, where $\mathcal{O}$ is the offset across all pixels in the chip, and $\mathcal{M}$ is the median of the chip (Section 3.1). To determine this systematic post calibration, we subtract out our correction map from the real data observed (=$\mathcal{O}$−correction map) in Figure 3 and recalculate the standard deviation of the offset per pixel. In Table 5, we see a ∼3 mmag improvement across both bands, which is substantial given that the initial effect is only ∼7 mmag.

A second magnitude error floor comes from the residual systematics on our inter-chip correction (Section 3.2). We find this by taking the standard deviation of the values presented in Figure 9 for each filter. Table 5 shows that our systematic uncertainty in error floor improves in both orange and cyan (by 15 and 13 mmag, respectively) after employing the inter-chip corrections.

Next, we quantify the systematic uncertainty related to the chromatic wavelength shifts applied to ATLAS passbands and validated by our HST CALSPEC and DAWD validation sets (Sections 3.2 and 6.1). We define this systematic uncertainty as: $\epsilon_{\rm chromatic} = \bar{\mathcal{A}}^{*}\mathcal{SN}$, where $\bar{\mathcal{A}}$ is the median slope across all chips, and $\mathcal{SN}$ is the observed SN Ia color range. This is practically propagated from the observed slope in the HST CALSPEC residuals using the SNe Ia color distribution ($-0.97 \leqslant g - i \leqslant -0.11$ mag at 2σ tails, covering 95% of the dataset) measured in Y. Murakami et al. (2026). Before our corrections, the median slopes for each filter are $\frac{\rm Residual}{g-i} \sim 0.029, 0.004$ for the cyan[14] and orange bands, respectively (see Figure 7). This corresponds to ∼0.026 and ∼0.003 mag-level changes in the zero-point across the color range of SNe Ia. The slope is consistent across our tertiary catalog and the primary, CALSPEC validation set. After applying our corrections derived from the tertiary star catalog, the remaining slope in the CALSPEC stars become considerably small (0.005), making the systematic uncertainty (See Table 5) consistent across filters $0.005\frac{\rm mag}{g-i\ \ \rm mag} \times (-0.11 - (-0.97))\ \ \rm mag \approx 0.0043$ mag.

Finally, we quantify our confidence in the absolute calibration of ATLAS using HST CALSPEC stars. We take the fitted offset (intercept of the slope at $g - i$ color = 0) after the wave shift has been calculated ($\mathcal{B}$). The systematic before calibration then is =Median($|\mathcal{B}|$) − δ_m. After calibration, it is =Median($|\mathcal{B}|$) − (interchip) − δ_m. This acts as an independent validation of only our inter-chip correction using primary calibrators. We specifically use data post-wave-shift correction for both the pre– and post–absolute calibration systematic, as the wave-shift systematic is already contained within row 3 of Table 5 (Section 6.3, Table 4). We find a 9 mmag and 1 mmag improvement for the orange and cyan bands, respectively.

Table 5 demonstrates that before our inter-chip, intra-chip, and wavelength corrections, there exists a total systematic uncertainty of 22 mmag and 35 mmag in the orange and cyan bands, respectively. After calibration, we are able to reduce this to 5 mmag and 10 mmag, respectively. For reasons discussed in Y. Murakami et al. (2026), we find that in *SNANA*, we must add a 10 mmag error floor to our TITAN SNe Ia already. This implies that our additional systematics from calibration are on a scale. What this means is that our calibration systematics do not significantly impact TITAN prospects for SN Ia cosmology.

6.4. Usage and Data Tools

The substantial work presented here can be reduced to a simple calibration pipeline shown in Figure 13. This flow chart shows our three calibration outputs, the pixel correction map (intra-chip), chip to chip ZP offsets (inter-chip), and transmission wavelength shifts. For the chip ZP offsets and the transmission wavelength shifts, these values can be lifted directly from Table 3 and applied to any ATLAS photometry files using the tools presented in the *ATLAST* (Y. Murakami & E. G. Marlin 2026) package of the data release. The pixel correction map produced here will also be available for download with DR1, and can be applied with a single line of python code from *ATLAST*.

Figure 13 also shows the validation sets used. The chip ZP offset and transmission wavelength-shift validations are discussed further in Sections 4.2 and 4.1, while the pixel correction map validation map is presented in Appendix C. For direct application to SN Ia light curves, please see

[14] The slope for the cyan band varies by a factor of a few between detectors. We use the median values for each filter as a representative value solely for the comparison with the post-correction size.

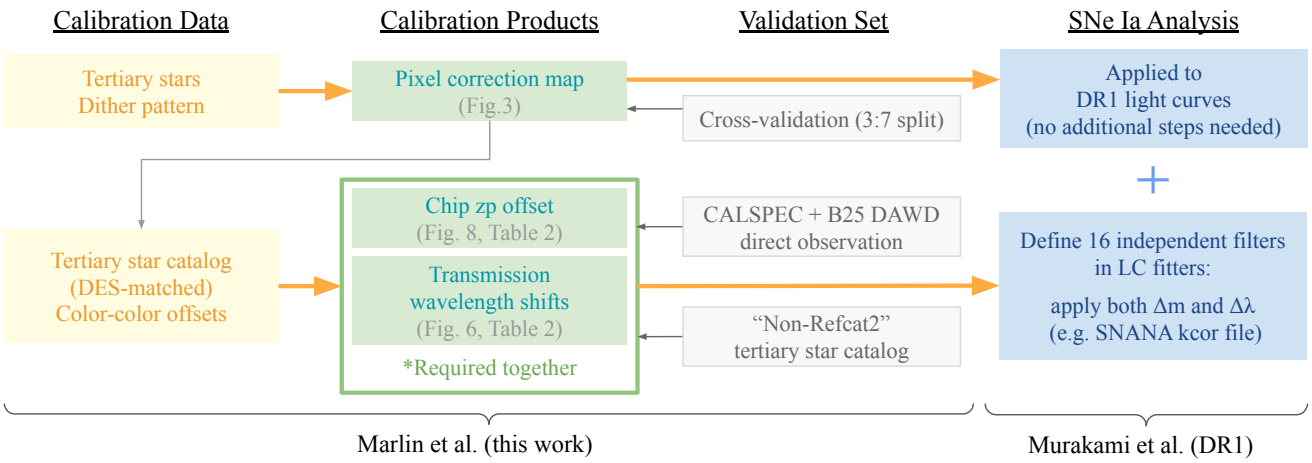

Figure 13. A summary of this work, products, and usage in future analysis. From left to right: dataset used in our analysis, calibration products (optimal calibration), dataset used to validate our calibration, and the methods to apply our calibration to SNe Ia light-curve analysis (e.g., SALT3 fitting).

Table 4
Slopes and Offsets Equivalent to Figure 10 for All Chips and Filters

Chip	$\Delta m_{\text{primary}}(o)$ (mag)	Primary Slope (o)	$\Delta m_{\text{primary}}(c)$ (mag)	Primary Slope (c)
0	-0.003 ± 0.014	$+0.001 \pm 0.005$	...	...
1	$+0.002 \pm 0.009$	$+0.001 \pm 0.005$	-0.012 ± 0.014	-0.013 ± 0.005
2	$+0.003 \pm 0.015$	$+0.011 \pm 0.005$	...	...
3	-0.001 ± 0.011	$+0.007 \pm 0.006$	-0.003 ± 0.022	-0.005 ± 0.007
4	$+0.010 \pm 0.011$	$+0.001 \pm 0.007$	-0.011 ± 0.016	-0.009 ± 0.005
5	$+0.005 \pm 0.010$	$+0.002 \pm 0.006$	-0.004 ± 0.012	-0.009 ± 0.005
6	-0.002 ± 0.011	$+0.005 \pm 0.004$	-0.006 ± 0.013	-0.000 ± 0.004
7	-0.001 ± 0.012	-0.007 ± 0.009	$+0.000 \pm 0.015$	-0.002 ± 0.010
8	$+0.023 \pm 0.013$	-0.011 ± 0.011	$+0.008 \pm 0.020$	-0.003 ± 0.016

Note. All values displayed here are post-inter-chip and post-wave-shift correction. These values are used in our second two systematics in Table 5.

Table 5
Average Systematic Uncertainty Values per Filter before and after Calibration

	Orange		Cyan		
Systematic	before	after	before	after	Description[a]
Intra-chip (pixel-to-pixel) variation	0.007	0.003	0.005	0.003	$\sigma(\Delta\text{ZP}_{\text{pixel}})$ in Figure 3
Inter-chip (chip-to-chip) variation	0.017	0.002	0.016	0.003	$\sigma(\langle\Delta\text{ZP}\rangle_{\text{chip}})$ in Figure 9
Chromatic Effect	0.005	0.004	0.029	0.005	Median slope ($\bar{\mathcal{A}}$) × SNe Ia color range (Section 6.3, Table 4)
Absolute Calibration	0.012	0.003	0.007	0.006	Median size of CALSPEC offsets, median Δm in Table 4
Total	**0.022**	**0.005**	**0.034**	**0.009**	

Notes. Values are in magnitude.
[a] Figures are cited here for reference purposes only, as they may only show measurements made before or after correction. We measure the same quantity before and after applying our correction models to quantify the reported values in this table.

Y. Murakami et al. (2026). All tools and calibration data can be downloaded from: https://titan-snia.github.io.

7. Conclusion

SNe Ia are a well-proven tool for measuring relative distances for use in cosmology. Until now, most major SN Ia cosmology surveys have relied on the same 200 low-z SNe Ia. TITAN now provides the largest, independent, spectroscopically confirmed low-z SNe Ia dataset to date. TITAN, which uses the ATLAS all-sky survey and data reduction pipelines (J. L. Tonry et al. 2018; L. Shingles et al. 2021), must be internally and externally calibrated before it can be used for cosmology. That calibration has been presented in this paper.

We conduct a relative calibration between ATLAS and DES, as DES is a well-measured southern-sky survey that contains stars both inside and outside of PS1 (the primary calibrating instrument of ATLAS Refcat2). We produced three distinct tertiary calibration star catalogs (Section 2.1) from the DES Y6 dataset: (1) a "color-blind" color-uniform sample from across the DES footprint matched to Refcat2 stars, (2) a "blue" sample that is intentionally biased substantially blue to

match the colors of low-z SNe Ia, and (3) a "non-Refcat2" sample of stars that exist in DES but that do not exist within Refcat2, which provides a completely independent dataset that mimics the behavior of SNe Ia in ATLAS. For each of these catalogs, we request ATLAS photometry from the server. We also generate synthetic data from HST CALSPEC, DAWD, and NGSL spectra.

We examine pixel-to-pixel variations *within* each ATLAS CCD and filter ("intra-chip") to build correction maps for each. We find most exhibit modestly small pixel-level structures below the 0.01 mag level, with the exception of chip 8o, where we notice a significant vignetting pattern (Figure 3). To account for the variations in pixel, we build a correction map. This is produced by binning the data, smoothing at an optimally calculated pixel radius (see Appendix C), then remapping to the 10,560 x 10,560 pixel CCD. We separately produce a map for each chip-filter combination.

We also compute corrections *across* each CCD and filter ('inter-chip'). We define this as the vertical offset in DES–ATLAS transformation and stellar color between the observed data and the synthetically produced data from NGSL (Figure 5), following the likelihood defined in Appendix A. Notably, the synthetic NGSL–real ATLAS residuals exhibit significant slopes in ATLAS cyan bands (Figure 7). Following B. Popovic et al. (2025), we correct for this by applying a shift in the wavelengths of the filters (Figure 8).

We validate our corrections in three ways: (1) with the independent "non-Refcat2" tertiary star catalog (Figure 9), (2) with independent primary and secondary absolute calibrators HST CALSPEC, and DAWD stars (Figure 10), and (3) by comparing distance moduli of cross-matched SNe Ia (Figure 12). All validation efforts point to improved consistency overall and reduced systematics (Table 5).

The calibration presented here serves as a baseline calibration, validation, and calibration-related systematic error budget for the upcoming TITAN DR1 cosmological analysis. The data release and all associated tools will be presented on the TITAN website.[15] The light curves, host galaxies, and simulations will be presented in Y. Murakami et al. (2026), J. Tweddle et al. (2026, in preparation), and J. Tweddle et al. (2026, in preparation), respectively.

Acknowledgments

This work has made use of data from the Asteroid Terrestrial-impact Last Alert System (ATLAS) project. The Asteroid Terrestrial-impact Last Alert System (ATLAS) project is primarily funded to search for near-Earth asteroids through NASA grants NN12AR55G, 80NSSC18K0284, and 80NSSC18K1575; byproducts of the NEO search include images and catalogs from the survey area. This work was partially funded by Kepler/K2 grant J1944/80NSSC19K0112 and HST-GO-15889, and STFC grants ST/T000198/1 and ST/S006109/1. The ATLAS science products have been made possible through the contributions of the University of Hawaii Institute for Astronomy, the Queen's University Belfast, the Space Telescope Science Institute, the South African Astronomical Observatory, and The Millennium Institute of Astrophysics (MAS), Chile, and the University of Oxford.

We would like to acknowledge the use of CasJobs in this work. The original JHU/ SDSS paper can be found here: W. OMullane et al. (2005).

We would like to thank John Tonry and the ATLAS team for assistance in gathering massive amounts of forced photometry and for their conversations and investigations into the difference imaging pipeline and nuances of the telescopes (especially chip 8o).

We thank the Hariri Institute at Boston University for their generous funding contributions to this project and for facilitating the space to hold a summer 2025 collaboration meeting.

D.O.J. acknowledges support from NSF grants AST-2407632, AST-2429450, and AST-2510993, NASA grant 80NSSC24M0023, and HST/JWST grants HST-GO-17128.028 and JWST-GO-05324.031, awarded by the Space Telescope Science Institute (STScI), which is operated by the Association of Universities for Research in Astronomy, Inc., for NASA, under contract NAS5-26555.

S.J.S. and K.W.S. acknowledge funding from STFC Grant ST/Y001605/1, a Royal Society Research Professorship and the Hintze Family Charitable Foundation.

This research has made use of the SVO2 Filter Profile Service "Carlos Rodrigo," funded by MCIN/AEI/10.13039/501100011033/ through grant PID2023-146210NB-I00.

Appendix A
Multicolor Joint Likelihood Analysis

In Section 3.2, we fit a single offset value to an ATLAS filter so that the empirical ATLAS–DES filter transformation matches synthetic prediction. This transformation is color-dependent, and there are multiple possible combinations of DES filters (e.g., `ATLAS-o→DES-g` as a function of color `DES-g-DES-i`). Each of the combination can be simultaneously evaluated to form a joint likelihood, and we describe the formalism of our likelihood function and the process to prepare necessary quantities below.

First, assuming that the DES filters and their star catalog values are well calibrated, we obtain an ATLAS offset for each (ith) star as the following:

$$\Delta_{\mathrm{i,\,x1,\,x2,\,y1,\,y2}} = m_{i,y1}^{\mathrm{ATLAS}} - m_{i,y2}^{\mathrm{DES}} - f_{y1\rightarrow y2}^{\mathrm{synth}}(m_{i,x1}^{\mathrm{DES}} - m_{i,x2}^{\mathrm{DES}}), \quad \text{(A1)}$$

where m represents the observed magnitudes of stars, with subscripts $y1$ for the ATLAS band of interest and $x1$, $x2$, $y2$ for the DES bands we use as a reference. Considering the overlaps of the sensitivity functions, we use the combinations of filters shown in Table 6. We note that there are two exceptions in the listed combinations: the dataset obtained with ($y1$, $y2$, $x1$, $x2$) = (c,g,g,r) is linearly identical to (c,r,g,r), and it causes the covariance matrix we describe later to be nearly singular. To avoid this issue and considering that it adds nearly no information, we exclude such combination. Similarly, another combination for the orange filter (o,i,r,i) is excluded. The synthetic transformation function between ATLAS filter $y1$ and DES filter $y2$ $f_{y1\rightarrow y2}^{\mathrm{synth}}$ is obtained by

[15] https://titan-snia.github.io

Table 6
Combinations of Filters Used for the Offset Analysis

	ATLAS-*c*				ATLAS-*o*			
#	*y*1	*y*2	*x*1	*x*2	*y*1	*y*2	*x*1	*x*2
1	ATLAS-*c*	DES-*g*	DES-*g*	DES-*r*	ATLAS-*o*	DES-*r*	DES-*g*	DES-*r*
2	ATLAS-*c*	DES-*g*	DES-*r*	DES-*i*	ATLAS-*o*	DES-*r*	DES-*r*	DES-*i*
3	ATLAS-*c*	DES-*g*	DES-*g*	DES-*i*	ATLAS-*o*	DES-*r*	DES-*g*	DES-*i*
4	ATLAS-*c*	DES-*r*	DES-*r*	DES-*i*	ATLAS-*o*	DES-*i*	DES-*g*	DES-*r*
5	ATLAS-*c*	DES-*r*	DES-*g*	DES-*i*	ATLAS-*o*	DES-*i*	DES-*g*	DES-*i*

fitting a third-order polynomial to a fully synthetic data m',

$$y \overset{fit}{=} f_{\rm synth} = {\rm Poly}_3(x),$$
$$x = m'_{x_1} - m'_{x_2}, \quad y = m'_{y_1} - m'_{y_2}. \tag{A2}$$

After evaluating Δ_i for each of the combination, we obtain a vector of offsets $\boldsymbol{r}_i = (\Delta_{i1}, \Delta_{i2}, \ldots, \Delta_{i5})^\top$. Due to repeated uses of data, these measurements are not independent of each other, and we quantify that effect by constructing a filter-to-filter covariance matrix for each star. Propagating uncertainties from each observed quantity in Equation (A1), we obtain a 5×5 matrix:

$$\begin{aligned}[\Sigma_i]_{jk} = &\underbrace{\sigma^2_{y_{1j}} + \sigma^2_{y_{2j}}\,\delta(y_{2j},\ y_{2k})}_{{\rm ATLAS}y_1 - {\rm DES}y_2 {\rm error}} \\ &+ \underbrace{f'_k\,\sigma^2_{y_{2j}}[\delta(y_{2j},\ x_{1k}) - \delta(y_{2j},\ x_{2k})] + f'_j\,\sigma^2_{y_{2k}}[\delta(y_{2k},\ x_{1j}) - \delta(y_{2k},\ x_{2j})]}_{y2-{\rm color}} \\ &+ \underbrace{f'_j f'_k\,\sigma^2_{x_{1j}}[\delta(x_{1j},\ x_{1k}) - \delta(x_{1j}, x_{2k})] - f'_j f'_k\,\sigma^2_{x_{2j}}[\delta(x_{2j},\ x_{1k}) - \delta(x_{2j},\ x_{2k})]}_{\rm color\text{-}color}.\end{aligned} \tag{A3}$$

Using this covariance matrix, we obtain appropriate weights between each measurement within $\boldsymbol{r}_i$ and collapse it into a single, representative offset value per star (generalized least-square estimation; GLS):

$$\bar{r}_i = \frac{\mathbf{1}^\top \Sigma_i^{-1}\mathbf{r_i}}{\mathbf{1}^\top \Sigma_i^{-1}\mathbf{1}},$$
$$\sigma^2_{\bar{r},i} = \frac{1}{\mathbf{1}^\top \Sigma_i^{-1}\mathbf{1}} \tag{A4}$$

where $\sigma^2_{\bar{r},i}$ is the variance for $\bar{r}_i$, and $\mathbf{1} = (1, 1, \ldots, 1)^\top$ is an all-one vector.

The obtained per-star offset value $\bar{r}_i$ and its variance $\sigma^2_{\bar{r},i}$ are then used to evaluate our likelihood, which accounts for possible combinations of filters, their uncertainties, covariances, and overlapping use of data across such combinations:

$$\ell(\Delta m_{\rm f},\ \sigma_{\rm int,f}) = \sum_i^{N_{\rm star}} -\frac{1}{2}\left[\frac{(\bar{r}_i - \Delta m_{\rm f})^2}{\sigma^2_{\bar{r},i} + \sigma^2_{\rm int}} + \ln(2\pi\sigma^2_{\bar{r},i} + 2\pi\sigma^2_{\rm int})\right]. \tag{A5}$$

This formula evaluates the likelihood of the proposed offset for the ATLAS filter $\Delta_{\rm f}$ (mag) against the par-star residual $\bar{r}_i$ (mag) for each ith star, which is derived from multiple combinations of filters between ATLAS and DES. We simultaneously measure the star-to-star intrinsic scatter $\sigma_{\rm int}$.

Appendix B
Profile Likelihood for Wavelength Shift

We estimate the optimal wavelength shift in the transmission functions (Figure 8) for each chip-filter combination using the profile likelihood method. When we allow the filter transmission function to have a small shift in the wavelength (which effectively changes the pivot wavelength and introduces/corrects the chromatic effect as described in Section 3.2), the color-averaged residual $\bar{r}_i$ in the likelihood function (Equation (A5)) becomes a function of wavelength-shift size $\Delta\lambda_{\rm filt}$. The updated log-likelihood is therefore

$$\ell(\Delta\lambda_{\rm f},\ \Delta m_{\rm f},\ \sigma_{{\rm int},f}) = \sum_i^{N_{\rm star}} -\frac{1}{2} \times\left[\frac{[\bar{r}_i(\Delta\lambda_{\rm f}) - \Delta m_{\rm f}]^2}{\sigma^2_{\bar{r},i} + \sigma^2_{\rm int}} + \ln(2\pi\sigma^2_{\bar{r},i} + 2\pi\sigma^2_{\rm int})\right], \tag{B1}$$

and this is computationally expensive, as each likelihood call requires the synthetic photometry of CALSPEC and DAWD stars to be calculated with updated filter functions. Outlier rejection is often necessary to account for poor observing conditions or poor PSF fit due to large proper motions, and varying data vector $\bar{r}_i$ makes it more difficult to retain a fixed, reproducible set of data while effectively rejecting outliers if one chooses to simply optimize all free parameters at once. We simplify this problem by evaluating profile likelihood along the $\Delta\lambda_{\rm f}$ space,

$$\ln P(\Delta\lambda_{\rm f}) = \ell(\Delta\lambda_{\rm f},\ \widehat{\Delta}m_{\rm f},\ \widehat{\sigma}_{{\rm int},f}) - \ell_{\rm max}, \tag{B2}$$

where $\ell(\Delta\lambda_{\rm f},\ \widehat{\Delta}m_{\rm f},\ \widehat{\sigma}_{{\rm int},f})$ is the likelihood maximized with a fixed $\Delta\lambda_{\rm f}$. Practically, this is evaluated over a grid of $\Delta\lambda_{\rm f}$

between $-150 \leqslant \Delta\lambda_f \leqslant 150$ Å with 1Å-spacing. The profile is then iteratively improved by applying an outlier rejection based on the maximum-likelihood set of $\bar{r}_i$ and using the same set of outlier-rejected stars across the grid. Once convergence of the profile is achieved, we fit a quadratic function to $\ln P(\Delta\lambda_f)$ to determine the best-fit offset $\Delta\lambda_{f,\mathrm{best}}$ and its uncertainty σ_λ, assuming Gaussian posterior. The typical size of the uncertainty is $\sigma_\lambda \lesssim 10$Å, and it corresponds to ∼mmag level of systematic, which is included in our analysis but is negligible compared to the estimated size of the systematic uncertainty from validation set.

Appendix C
Optimal Smoothing Radius Determination

To determine our optimal smoothing radius for the intra-chip correction, we trained a model on 70% of the data from our calibration stars and then validated it with the remaining 30%. This process is done on each chip/filter combo, and the split is regenerated randomly four times for each combo. This results in Figure 14, which shows the reduced χ^2 as a function of smoothing radius. You can see that most of the chips are in the 250–750 pixel smoothing radius range for minimum reduced chi squared.

Our model functions as follows: it bins the data into 50×50 pixel chunks. It then convolves the binned data with a Gaussian kernel (it ignores edge effects, as these have a higher likelihood of being inaccurate by definition). Our model then uses the large-scale structure of the CCD to correct for systematic offsets in the photometric residuals across the chip.

We used Figure 14 to determine a median minimum χ^2 across all chips, for which smoothing radius we should use for our correction model. We then apply the smoothing function to the dataset, which provides a correction to the dataset specifically correcting the chip 8 data without changing the rest of the chips data in a nonuniform way. This produces our intra-chip correction.

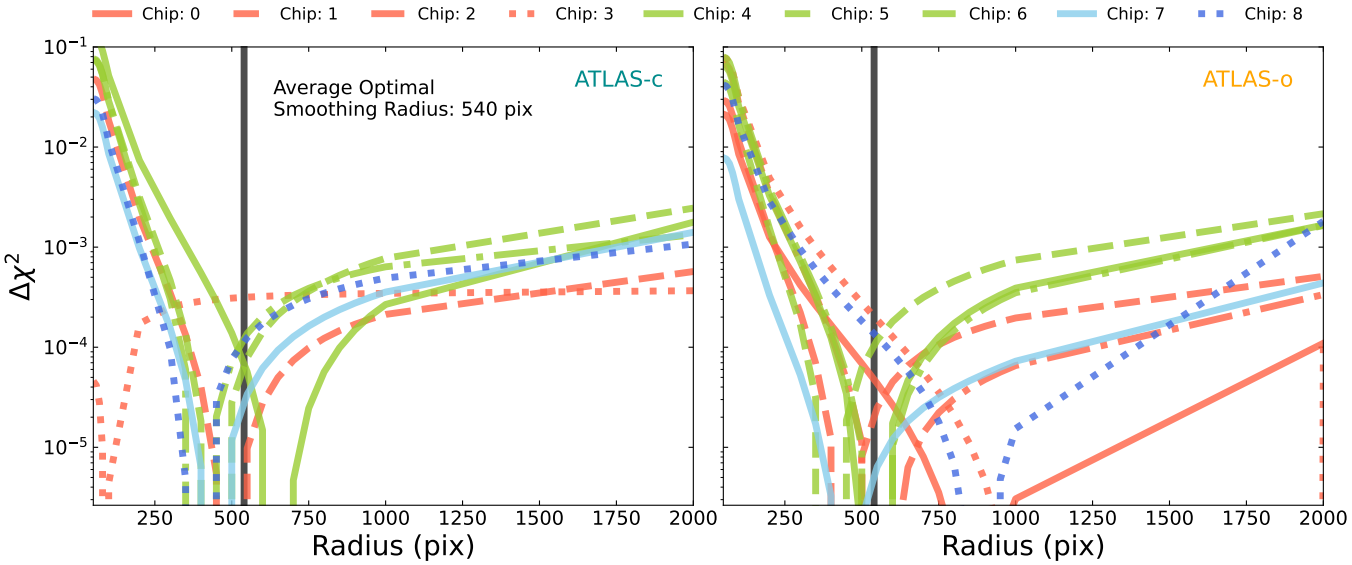

Figure 14. Cross-validation plot of reduced χ^2 vs. smoothing radius in pixels. You can see the smoothing radius that minimizes the χ^2 is focused around 540 pixels. We would rather slightly over-bin (thus, under-correct) than under-bin, which would result in over-correcting, leading to potentially misleading and unrealistic trends. The y-axis is the reduced χ^2 minus the minimum χ^2 for each chip-filter combo.

ORCID iDs

Elijah G. Marlin https://orcid.org/0009-0003-4631-3184
Yukei S. Murakami https://orcid.org/0000-0002-8342-3804
Dillon Brout https://orcid.org/0000-0001-5201-8374
Jack W. Tweddle https://orcid.org/0009-0004-5681-545X
Brodie Popovic https://orcid.org/0000-0002-8012-6978
Ken W. Smith https://orcid.org/0000-0001-9535-3199
Stephen J. Smartt https://orcid.org/0000-0002-8229-1731
Daniel M. Scolnic https://orcid.org/0000-0002-4934-5849
David Jones https://orcid.org/0000-0002-6230-0151
Erik R. Peterson https://orcid.org/0000-0001-8596-4746
Adam G. Riess https://orcid.org/0000-0002-6124-1196
Maria Vincenzi https://orcid.org/0000-0001-8788-1688
Nora F. Sherman https://orcid.org/0000-0001-5399-0114
Maria Acevedo https://orcid.org/0000-0002-5389-7961
Jasper Milstein https://orcid.org/0009-0002-7557-0406
Mitchell Dixon https://orcid.org/0000-0003-0928-0494
Armin Rest https://orcid.org/0000-0002-4410-5387

References

Abbott, D. C. T. M. C., Acevedo, M., Aguena, M., et al. 2024, ApJL, 973, L14
Acevedo, M., Sherman, N. F., Brout, D., et al. 2026, ApJ, 996, 7
Aleo, P. D., Malanchev, K., Sharief, S., et al. 2023, ApJS, 266, 9
Bechtol, K., Sevilla-Noarbe, I., Drlica-Wagner, A., et al. 2026, ApJS, 282, 62
Bernstein, G. M., Armstrong, R., Plazas, A. A., et al. 2017, PASP, 129, 074503
Bohlin, R. C., Gordon, K. D., & Tremblay, P. E. 2014, PASP, 126, 711
Boruah, S. S., Hudson, M. J., & Lavaux, G. 2020, MNRAS, 498, 2703
Boyd, B. M., Narayan, G., Mandel, K. S., et al. 2025, MNRAS, 540, 385
Brout, D., Scolnic, D., Kessler, R., et al. 2019, ApJ, 874, 150
Brout, D., Scolnic, D., Popovic, B., et al. 2022a, ApJ, 938, 110
Brout, D., Taylor, G., Scolnic, D., et al. 2022, ApJ, 938, 111
Brout, D., Taylor, G., Scolnic, D., et al. 2022b, ApJ, 938, 111
Brown, P. J., Breeveld, A. A., Holland, S., Kuin, P., & Pritchard, T. 2014, Ap&SS, 354, 89
Burke, D. L., Rykoff, E. S., Allam, S., et al. 2017, AJ, 155, 41
Chen, P., Dong, S., Kochanek, C. S., et al. 2022, ApJS, 259, 53
DESI Collaboration, Abdul Karim, M., Aguilar, J., et al. 2025, PhRvD, 112, 083515
Dilday, B., Smith, M., Bassett, B., et al. 2010, ApJ, 713, 1026
Filippenko, A. V. 2005, in Astrophysics and Space Science Library, Vol. 332, White Dwarfs: Cosmological and Galactic Probes, ed. E. M. Sion, S. Vennes, & H. L. Shipman (Springer), 97
Flewelling, H. A., Magnier, E. A., Chambers, K. C., et al. 2020, ApJS, 251, 7
Foley, R. J., Koekemoer, A. M., Spergel, D. N., et al. 2018b, arXiv:1812.00514
Foley, R. J., Scolnic, D., Rest, A., et al. 2018a, MNRAS, 475, 193
Gaia Collaboration, Brown, A. G. A., Vallenari, A., et al. 2018, A&A, 616, A1
Ganeshalingam, M., Li, W., Filippenko, A. V., et al. 2010, ApJS, 190, 418
Hamuy, M., Phillips, M. M., Suntzeff, N. B., et al. 1996, AJ, 112, 2438
Henden, A. A., Templeton, M., Terrell, D., et al. 2016, yCat, 2336, 0
Hicken, M., Challis, P., Jha, S., et al. 2009a, ApJ, 700, 331
Hicken, M., Challis, P., Kirshner, R. P., et al. 2012, ApJS, 200, 12
Hicken, M., Wood-Vasey, W. M., Blondin, S., et al. 2009b, ApJ, 700, 1097
Jha, S., Kirshner, R. P., Challis, P., et al. 2006, AJ, 131, 527
Kessler, R., Bernstein, J., Cinabro, D., et al. 2009, PASP, 121, 1028
Koleva, M., & Vazdekis, A. 2012, A&A, 538, A143
Krisciunas, K., Contreras, C., Burns, C. R., et al. 2017, AJ, 154, 211
Lacroix, L., Regnault, N., de Jaeger, T., et al. 2025, arXiv:2509.04073
Licandro, J., Tonry, J., Alarcon, M. R., Serra-Ricart, M., & Denneau, L. 2023, in 2nd NEO and Debris Detection Conf., 2
Magnier, E. A., Schlafly, E. F., Finkbeiner, D. P., et al. 2020, ApJS, 251, 6
Marriner, J., Bernstein, J. P., Kessler, R., et al. 2011, ApJ, 740, 72
Murakami, Y., & Marlin, E. G. 2026, ATLAST (ATLAS Transient Lightcurve Analysis and Smoothing Tools), v1, Zenodo, doi:10.5281/zenodo.18763546
Murakami, Y., Tweddle, J., Marlin, E., et al. 2026
Newman, M. J. B., Larison, C., Jha, S. W., et al. 2025, arXiv:2508.20023
OMullane, W., Li, N., Nieto-Santisteban, M., et al. 2005, arXiv:cs/0502072
Phillips, M. M. 1993, ApJL, 413, L105
Popovic, B., Kenworthy, W. D., Ginolin, M., et al. 2025, arXiv:2506.05471
Riess, A. G., Kirshner, R. P., Schmidt, B. P., et al. 1999, AJ, 117, 707
Riess, A. G., Yuan, W., Macri, L. M., et al. 2022, ApJL, 934, L7
Rigault, M., Smith, M., Goobar, A., et al. 2025, A&A, 694, A1
Rubin, D., Aldering, G., Betoule, M., et al. 2025, ApJ, 986, 231
Rykoff, E., Tucker, D., Burke, D., et al. 2023, The Dark Energy Survey Six-Year Calibration Star Catalog, OSTI, US Dept. Energy
Sanderson, R. E., Hickox, R., Hirata, C. M., et al. 2024, arXiv:2404.14342
Schlafly, E. F., Finkbeiner, D. P., Jurić, M., et al. 2012, ApJ, 756, 158
Scolnic, D., Brout, D., Carr, A., et al. 2022, ApJ, 938, 113
Scolnic, D., Casertano, S., Riess, A., et al. 2015, ApJ, 815, 117
Sherman, N. F., Acevedo, M., Brout, D., et al. 2026, ApJ, 1002, 146
Shingles, L., Smith, K. W., Young, D. R., et al. 2021, TNSAN, 7, 1
Smith, K. W., Smartt, S. J., Young, D. R., et al. 2020, PASP, 132, 085002
Sonnett, S., Meech, K., Jedicke, R., et al. 2013, PASP, 125, 456
Stahl, B. E., Zheng, W., de Jaeger, T., et al. 2019, MNRAS, 490, 3882
Sánchez, B. O., Brout, D., Vincenzi, M., et al. 2024, ApJ, 975, 5
Tang, X. T., Brout, D., Karwal, T., et al. 2025, ApJL, 983, L27
Tonry, J. L., Denneau, L., Flewelling, H., et al. 2018, ApJ, 867, 105
Tonry, J. L., Denneau, L., Heinze, A. N., et al. 2018, PASP, 130, 064505
Tripp, R. 1998, A&A, 331, 815
Vincenzi, M., Brout, D., Armstrong, P., et al. 2024, ApJ, 975, 86
Wolf, C., Onken, C. A., Luvaul, L. C., et al. 2018, PASA, 35, e010